High-n Rydberg Transition Spectroscopy for Heavy Impurity Transport Studies in W7-X

Colin Swee,[1, a)] Benedikt Geiger,[1] Oliver Ford,[2] Martin O'Mullane,[3] Peter Poloskei,[2] Felix Reimold,[2] Thilo Romba,[2] Thomas Wegner,[2] and W7-X Team[2, b)]

[1)] *Department of Engineering Physics, University of Wisconsin Madison, Madison, WI, 53706, USA*

[2)] *Max-Planck Institute for Plasma Physics, 17491, Greifswald, Germany*

[3)] *University of Strathclyde, 107 Rottenrow, Glasgow G40N, United Kingdom*

(Dated: April 2024)

Here, we present a novel spectroscopy approach to investigate impurity transport by analyzing line-radiation following high-n Rydberg transitions. While high-n Rydberg states of impurity ions are unlikely to be populated via impact excitation, they can be accessed by charge exchange (CX) reactions along the neutral beams in high-temperature plasmas. Hence, localized radiation of highly ionized impurities, free of passive contributions, can be observed at multiple wavelengths in the visible range. For the analysis and modeling of the observed Rydberg transitions, a technique for calculating effective emission coefficients is presented which can well reproduce the energy dependence seen in datasets available on the OPEN-ADAS database. By using the rate coefficients and comparing modeling results with the new high-n Rydberg CX measurements, impurity transport coefficients are determined with well documented 2σ confidence intervals for the first time. This demonstrates that high-n Rydberg spectroscopy provides important constraints on the determination of impurity transport coefficients. By additionally considering Bolometer measurements which provide constraints on the overall impurity emissivity and therefore impurity densities, error bars can be reduced even further.

I. INTRODUCTION

The reliable characterization and control of impurity transport in fusion plasmas is important to ensure favorable fusion reactor performance. If the build-up of heavy impurities is not mitigated, they can cause severe radiative cooling, limiting plasma temperatures and reducing fusion reaction rates via fuel dilution. Therefore, the development of diagnostic methods for detailed impurity transport studies is necessary to determine plasma scenarios to be used in future fusion power plants.

Often the goal for impurity transport studies is to determine the impurity diffusion and convection coefficients which govern the radial impurity fluxes. These fluxes can be described by the radial transport equation:

$$\frac{\partial n_z}{\partial t} = \frac{1}{r}\frac{d}{dr}r\left(D\left(r\right)\frac{dn_z}{dr} - v\left(r\right)n_z\right) + S - Q, \quad (1)$$

where n_z is the density of an impurity with charge Z, D is the diffusion coefficient, and v is the convection velocity. S and Q represent source and sink terms such as ionization, recombination, and losses in the open field region.

So far, the main workhorse diagnostics for heavy impurity transport studies have been vacuum ultraviolet (VUV) and soft X-ray spectroscopy[1–4] which provide line integrated radiation of heavy impurity ions with time-resolutions in the range of 1 ms. This is sufficient to resolve the radiation emitted after dedicated impurity injections such as by the laser blow-off technique. By comparing the evolution of the measured line radiation with forward modeling results e.g. by STRAHL or AURORA, diffusion and convection profiles have been determined[5–7]. However, results remain fairly insensitive to the modeled impurity convection velocity specifically, explained by the poor spatial localization of the line integrated measurements[6]. Since radial transport of impurities significantly modifies their ionization balance, the simple coronal model which relates a given impurity line emission to a local temperature, and hence, radial position, is typically not applicable. Therefore, well localized measurements are needed to further improve the measurement constraints on the impurity density profile shapes and therefore the D and v profiles.

One method to obtain localized information on impurity ions is charge exchange recombination spectroscopy (CXRS). This technique makes use of the charge exchange reaction which is characterized by a donor-neutral from a neutral beam providing an electron to an impurity ion which in turn emits localized line radiation. The charge exchange process has a high probability to populate a highly excited state which yields radiation that is hardly observed following electron impact excitation processes. CXRS measurements of intrinsic impurities are routinely performed to study the density and profile shape of elements such as Carbon[8–10]. In addition, CXRS measurements of heavy impurity ions were performed at TFTR in 1991[11] but followup studies have been limited since then.

Recently, a new diagnostic hardware has been installed at W7-X which collects absolutely calibrated, localized radiation along one the experiment's heating neutral beam paths and analyzes radiation in the vis-

---

[a)] Author to whom correspondence may be addressed: ckswee@wisc.edu

[b)] See T.S. Pedersen *et al* 2022 Nucl. Fusion 62 042022 for the full list of W7-X team members.

ible range with a frame rate of 1 kHz[12], fast enough to resolve impurity transport time scales. It has been shown recently that this system can provide diffusion and convection profiles with reasonable error bars by using the pySTRAHL code incorporated into a Bayesian framework[13]. Here, we present a detailed overview of the employed high-n Rydberg transition spectroscopy as well as a method to accurately model emission intensities by calculating charge exchange rate coefficients based on using a reduced collisional-radiative model. Additionally, it is demonstrated that the new high-n Rydberg spectroscopy method, in combination with other diagnostics such as bolometry, provides high-quality impurity transport profiles.

The structure of the remainder of this work is as follows: In section II, the observation of High-n Rydberg-like transitions in the spectral range of 500 nm is discussed along with a prediction for several other lines which could be explored in future studies. Section IIIA discusses the forward model considered for simulating CXRS measurements and in section IIIB, a method is presented for calculating the effective emission coefficients necessary to model the signal intensities. Section 4 then presents the Bayesian statistical model used to infer the impurity transport coefficients. Section 5 provides inference results including a discussion of fitting uncertainties which are affected by the complexity of the CXRS forward model. Also in section 5, the addition of radiated power measurements into the inference framework is presented along with their effect on the fitting uncertainty. Finally, section 6 provides a summary of the presented work along with a conclusion and avenues for future studies.
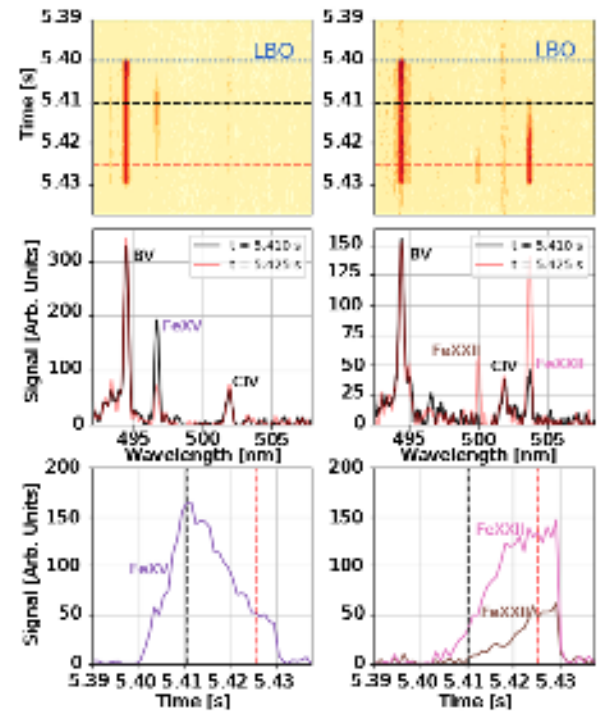

FIG. 1. Example of observed Rydberg-like emissions following an LBO injection. The left column depicts emission along a line of sight near the plasma edge while that on the right shows emission further into the plasma. The top panels depicts the emission intensity in the color scale vs. wavelength and time, the middle panels show intensity vs. wavelength at two separate times, and the bottom panels show the signal intensity vs. time. The time slices depicted in the middle panels are shown with dashed lines in the top and bottom panels.

II. OBSERVATION OF HIGH-N RYDGERG-LIKE TRANSITIONS

High n-Rydberg emissions have been routinely observed and studied during the 2023 experimental campaign at W7-X. The evolution of example spectra obtained during a representative experiment with 2 MW of ECRH, a line averaged electron density of $\sim 1.5 \times 10^{19} \text{m}^{-3}$, and a core electron temperature of ~ 4 keV are depicted in Fig. 1. Signals from two different lines of sights observing CX emission show a clear effect following a laser blow-off (LBO)[14,15] injection of iron atoms. The different emission lines appearing in the spectra exhibit different temporal characteristics which demonstrates that the emission lines originate from different charge states and radial positions.

The observed wavelength can be reproduced very well by the relativistic Rydberg formula recently derived in 16:

$$\frac{1}{n_{air}\lambda_{air}} = \frac{m_e c}{h} \left(\frac{1}{\sqrt{1 - (q+1)^2 \alpha^2 / n_2^2}} - \frac{1}{\sqrt{1 - (q+1)^2 \alpha^2 / n_1^2}} \right) \quad (2)$$

Here n_{air} is the index of refraction in air, λ_{air} is the wavelength observed in air, m_e is the mass of the electron, c is the speed of light, h is the Planck constant, q is the net charge of the ion, and α is the fine structure constant. n_1 and n_2 are the upper and lower energy levels of the transition respectively.

The analysis of high-n transitions provides several benefits when compared to other spectroscopy methods. First, since the energy levels populated by the charge exchange process are so high[17] (n $\gtrsim q^{3/4}$), they are excessively unlikely to be reached by electron impact excitation processes, the usual source of passive radiation inside the confined region. For this reason, as long as the background neutral density is sufficiently low, observed high-n Rydberg emissions are free of passive contributions, greatly simplifying their analysis. The second ad-

vantage of the high-n Rydberg method is that equation 1 only depends on the energy levels and the ion effective charge. Hence, the diagnostic method is agnostic to the particular impurity species. This can present complications if multiple heavy impurities are present at the same time however, it can also be an advantage in injection studies which introduce different elements one at a time as it greatly simplifies line identification. The final benefit of this analysis method is that of the relative engineering simplicity of utilizing CXRS. Since observed emissions are in the visible range, standard lens and optical fiber setups can be utilized, something that is not possible when observing VUV or soft x-ray emissions. Therefore, the high-n Rydberg spectroscopy is particularly powerful when performing impurity transport studies based on dedicated impurity injections.

While previous studies have focused on high-n Rydberg emissions in the spectral range of 490 - 510 nm, equation 1 can be used to predict high-n transitions throughout the visible spectrum. In fact, iterating through possible values of q, n_1, and n_2, indicates the possibility of several hundred line transitions between 350 nm and 750 nm. Table I shows the expected wavelengths following all possible $\Delta n = 1$ transitions and charge states between Z=20 and Z=50. Whether these charge states are observable depends on the ionization balance of the impurity species being analyzed. For example, impurities such as iron have a limited number of electrons so only charge states up to Z=26 exist. For very heavy impurities such as tungsten many charge states could potentially exist throughout the plasma volume and the charge balance strongly depends on the temperature range. Figure 2 shows a histogram describing the coronal charge state equilibrium of both iron and tungsten at a temperature of 2 keV and a density of 5×10^{19} m^{-3}. As can be seen, Fe would primarily cause Z=23+ and Z=24+ radiation, while W would have a broader distribution centered around Z=40.

In addition, the strength of the various line emissions depends on whether the upper energy level for a particular transition will be likely to be populated following charge exchange. Typically, partial cross-sections for CX into particular energy levels peak 2-5 energy levels above the estimate of $n_{upper} \sim q^{3/4}$[18]. The higher the beam energy, the more slowly these cross-sections fall off as one goes towards higher n therefore allowing for appreciable population of even higher energy levels[17]. For a fairly standard NBI injection energy of 50 - 100 keV, energy levels for which visible wavelength transitions occur are readily populated.
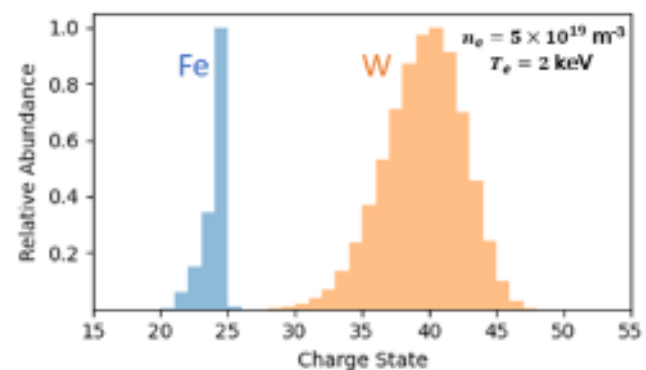

FIG. 2. Histogram of the relative abundance of various charge states in a coronal equilibrium for a plasma with $n_e = 5 \times 10^{19}$ m-3 and $T_e = 2$ keV. ADAS files used for this calculation: "acd89_fe.dat", "scd89_fe.dat", "acd01_w.dat", and "scd01_w.dat"

III. MODELING OF ACTIVE IMPURITY CHARGE EXCHANGE EMISSION

A. CXRS Forward Model

The equation for the emission seen along a given sightline is:

$$\epsilon_{LOS} = \int n_q \sum_k \sum_E n_{k,E} \varepsilon_{k,E} \, dl \quad (3)$$

Here n_q is the impurity density for charge state q and the sum over k and E represents the sum over the neutral excited states and beam energy components respectively with $k = 1$ corresponding to the ground state of the beam neutrals. $n_{k,E}$ is the neutral density of excited state k and energy component E which comprises of the full, half, and third components as well as the NBI halo. Note that these beam energy components arise from the acceleration of H_1^+, H_2^+, and H_3^+ ions prior to neutralization in the beam. The halo component in turn, arises from the charge exchange between main plasma ions and the beam neutrals leading to a thermalized population of neutrals in the beam vicinity. For modeling of these densities, the pySTRAHL[9] and pyFIDASIM[19] codes are available. For a user-defined set of kinetic profiles, magnetic geometry, and source term, pySTRAHL solves the impurity transport equation (eq. 1) for the impurity densities, n_q, as a function of time, position, and charge state. To simulate the neutral densities, the pyFIDASIM code utilizes a collisional-radiative model in a Monte-Carlo simulation that tracks the evolution of injected beam neutrals as they interact with the background plasma. Given a set of input kinetic profiles, a magnetic geometry, and the relevant beam parameters, pyFIDASIM then calculates the neutral densities, $n_{k,E}$ as a function of position, energy component, and excitation level. Finally, $\varepsilon_{k,E}$ represents the effective emission coefficient for a given energy

Wavelength [nm]	q	n_{upper}	Wavelength [nm]	q	n_{upper}	Wavelength [nm]	q	n_{upper}	Wavelength [nm]	q	n_{upper}
400.22	45	26	467.38	49	29	542.26	32	23	622.31	38	27
401.01	28	19	467.40	44	27	544.22	43	28	625.06	49	32
407.79	30	20	470.49	30	21	544.34	22	18	626.79	40	28
408.08	42	25	471.60	39	25	546.29	34	24	627.06	24	20
408.93	37	23	475.90	32	22	551.20	36	25	631.98	42	29
410.79	47	27	476.95	46	28	552.22	45	29	637.57	22	19
415.18	32	21	480.11	41	26	552.60	20	17	637.77	44	30
418.21	44	26	482.05	34	23	556.83	38	26	644.07	46	31
418.23	39	24	486.66	48	29	560.52	47	30	650.83	48	32
421.42	49	28	488.82	36	24	563.07	40	27	652.77	33	25
421.93	21	16	488.89	43	27	569.09	49	31	652.97	20	18
423.05	34	22	**496.10***	**38**	**25**	569.83	42	28	653.51	35	26
423.07	23	17	**497.92***	**45**	**28**	575.85	29	22	653.54	31	24
425.95	25	18	**498.91***	**25**	**19**	576.69	31	23	655.50	37	27
427.75	41	25	499.87	27	20	576.72	27	21	656.16	29	23
428.46	46	27	**499.91***	**23**	**18**	577.04	44	29	658.53	39	28
430.17	27	19	**502.38***	**29**	**21**	578.91	33	24	661.07	27	22
431.34	36	23	**503.50***	**21**	**17**	579.75	25	20	662.44	41	29
435.44	29	20	503.82	40	26	582.25	35	25	667.09	43	30
437.44	43	26	506.11	31	22	584.63	46	30	668.87	25	21
438.80	48	28	**507.15***	**47**	**29**	585.54	23	19	672.39	45	31
439.96	38	24	510.83	33	23	586.52	37	26	678.24	47	32
441.53	31	21	511.90	42	27	591.58	39	27	680.41	23	20
447.30	45	27	516.36	35	24	592.56	48	31	684.57	49	33
448.31	33	22	516.57	49	30	594.95	21	18	691.40	34	26
448.87	40	25	520.30	44	28	597.30	41	28	691.42	36	27
455.64	35	23	522.56	37	25	603.57	43	29	692.74	38	28
457.28	47	28	528.97	46	29	610.33	45	30	692.94	32	25
458.03	42	26	529.33	39	26	614.50	30	23	695.15	40	29
460.66	22	17	536.57	41	27	614.53	32	24	696.39	30	24
460.72	24	18	537.59	26	20	616.00	34	25	696.85	21	19
462.63	26	19	537.63	28	21	616.26	28	22	698.48	42	30
463.08	20	16	537.87	48	30	617.51	47	31			
463.43	37	24	539.29	30	22	618.66	36	26			
465.99	28	20	539.62	24	19	620.24	26	21			

TABLE I. $\Delta n = 1$ line transitions with wavelengths calculated via equation 2 in the visible range. Those transitions that have been seen in experiments at W7-X are indicated in bold text with an asterisk.

component and neutral excited state.

Many of these emission coefficients are tabulated in atomic data repositories for light to medium impurities, however, for heavier impurities, few datasets are available. To simplify equation 3, one can make notes of trends from the heaviest dataset available, argon[20] which we assume to hold for the analysis of iron. In particular, one can note that for a 50 keV/amu beam that undergoes charge exchange with argon, the third energy component ($E = 3$) and beam halo with $k = 1$ exhibit a very small effective emission coefficient. The halo emission coefficient for the $k = 2$ excited state can potentially be comparable or even slightly larger than the emission coefficient of the $k = 1$ first energy component however, in the simulations performed in this work, the neutral densities of the $k = 2$ excited states were found to be two to three orders of magnitude smaller than the corresponding $k = 1$ populations. Neglecting these small terms in equation 3

simplifies it to the following form where only the first two neutral excited states are considered for the full and half energy components:

$$\epsilon_{LOS} \approx \int n_Z \left(n_{k=1,full}\varepsilon_{k=1,full} + n_{k=1,half}\varepsilon_{k=1,half} \right) dl$$

(4)

The process used to calculate the effective emission coefficients typically involves an integration over the relative collision velocities between beam neutrals and the impurities. Here, we note that the beam velocity is much larger than the thermal velocity of the ions such that we can treat the distribution as a delta function centered at the beam velocity. This allows one to pull the emission coefficients outside of the integral since it approximately does not depend on the local plasma parameters:

$$\epsilon_{LOS} \approx \varepsilon_{k=1,full} \int n_Z n_{k=1,full} dl$$
$$+ \varepsilon_{k=1,half} \int n_Z n_{k=1,half} dl \tag{5}$$

Simplifying the model in this way allows one to go from considering a total of 6 emission coefficients at each point along the line of sight down to just 2 emission coefficients which are assumed constant along the line of sight.

B. Determination of Effective Emission Coefficients

To determine the emission coefficients for the two energy levels relevant to our measurements of iron, a strategy similar to that described in reference 21 is utilized.

Assuming that the energy level balance for a particular impurity ion is in steady state, the balance between its populating and depopulating mechanisms can be written as:

$$\frac{dn_{z,k}}{dt} = 0 \approx -n_{z,k} \sum_{i<k} A_{k\to i} + \sum_{i>k} n_{z,i} A_{i\to k}$$
$$+ n_{z+1,gr} \langle \sigma_{z+1,gr\to k} v_{rel} \rangle n_0 \tag{6}$$

Here, k denotes an energy level of interest, A represents the Einstein coefficients for transition between one energy level and another, and $n_{z,x}$ represents the number density of an ion with charge z in energy level x. $\sigma_{z+1,gr\to k}$ is the cross-section for charge exchange electron capture between a ground state ion with charge $z+1$ and a neutral which leaves the recombined ion in energy level k. v_{rel} is the relative velocity of the impurity ion and the neutral and the angle brackets represent an integration over the velocity distribution. Finally, n_0 is the number density of the ground state neutral density for the main plasma species. The terms on the right-hand side of equation 6 correspond to (from left to right) depopulation via spontaneous decay to lower energy levels, population via spontaneous decay from upper energy levels, and population via charge exchange between a ground state impurity ion and a fuel neutral. Note that we neglect several terms in this energy level balance including collisional excitation and de-excitation as well as three body recombination which are very small for high-n states. We also drop terms that would include contributions from radiative and dielectric recombination which are small for the electron temperatures considered here. Additionally, collisional ionization is not considered as it takes place on time scales much longer than those considered here for highly ionized impurities.

Since each of the energy level populations are coupled via equation 6, one can write out a matrix equation that describes the steady state balance of each energy level. The effective emission coefficients that appear in equation 5 for the transition between states $q \to p$ are then $\varepsilon = n_{z,q} A_{q\to p}/n_{z+1,gr} n_0$. This term can be evaluated

by dividing equation 6 by $n_{z+1,gr} n_0$ and inverting the matrix.

To solve equation 6, n and l resolved Einstein A coefficients have been calculated using the Autostructure code[22] which solves the wave-function using a Slater approach. Moreover, n-resolved cross sections for charge exchange into the various energy levels considered in equation 6 can be determined from a universal cross-section scaling similar to what is performed in reference 21. It is then assumed that following charge exchange into the relevant n-level, collisional redistribution populates each unique n, l state according to their statistical weights. Bench-marking results showing the comparison of effective emission coefficients calculated using this method and those available on OPEN ADAS are given in figure III B for a range of beam energies representative of the energy ranges used in most experiments. The values found on the ADAS database are given by the hollow squares while those calculated using our presented method are shown by the lines with overlayed error bars. Note that the energy dependence for each transition matches the ADAS datasets well while a scaling factor must be introduced to match the magnitude. This scaling factor along with labels indicating the transition energy levels are annotated next to the corresponding plotted data. However, this scaling factor does not enter into the inferences performed in section IV since for this work, we will be fitting our model to relatively calibrated charge exchange signals. Since we are assuming that the effective emission coefficients are approximately only a function of beam energy, the total emission seen by each line of sight will be a linear combination of the effective emission coefficients for the full and half energy components multiplied times the local full and half beam densities. Therefore, in order to accurately capture the relative intensity between lines of sight, only knowledge of the ratio between the full and half energy effective emission coefficients is necessary. Plotted ADAS adf12 data is taken from the following files: *qef93#h_ne10.dat*, *qef07#h_arf#ar17.dat*, *qef07#h_arf#ar18.dat*.

The calculated effective emission coefficients used in the modeling of the Fe XXII and Fe XXIV signals are then given in figure 4 as a function of the beam energy. Additionally, a single ADAS calculation was acquired for the Fe XXIV transition (file: *qef07#h_arf#fe24.dat*) which is additionally plotted next to the newly calculated emission coefficients. Again, the calculated datasets are scaled up to easily compare the energy dependence to the existing data.

IV. BAYESIAN FRAMEWORK

Bayesian inference can be utilized in a manner similar to least squares optimization methods to determine the most likely set of parameters that describe a given set of observations. Here we compare the evolution and relative intensity of the measured high-n Rydberg emission
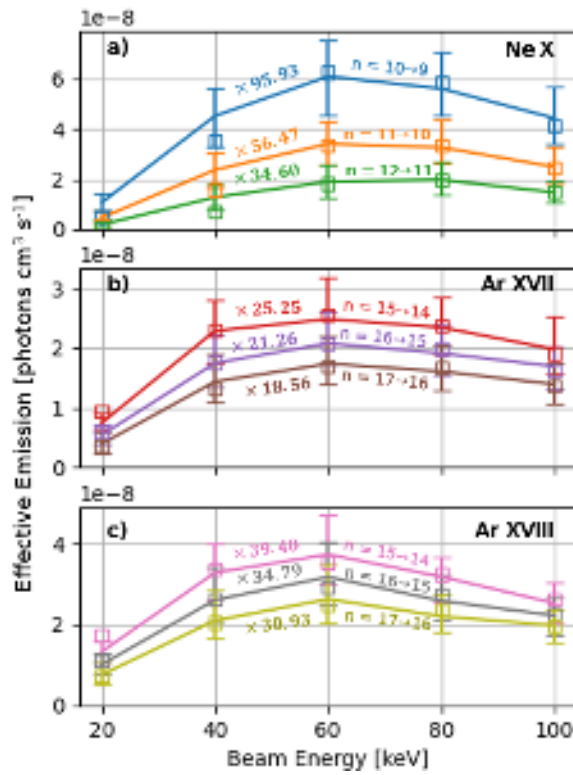
FIG. 3. Calculated charge exchange effective emission coefficients for a) Ne^{10+}, b) Ar^{17+}, c) Ar^{18+} plotted as a function of beam energy with error bars indicating fitting uncertainty. Each set of calculated data must be multiplied by a scaling factor (annotated next to each set data) to match the coefficients from the corresponding ADAS ADF12 datasets (shown in hollow squares).

with forward modeled results within a Bayesian framework that aims at identifying D and V profiles. To fully define the Bayesian framework used, first a set of prior constraints must be described. Both the impurity diffusion and the peaking ratio rV/D are parameterized with piece-wise cubic-Hermite interpolation polynomials. Two knot points are located near the core and the edge with a third free to vary in position between the two. The core and edge knot points for the diffusion and peaking ratio profiles are slightly offset from one another to encourage the model to decouple the two contributions to the transport. The magnitude of the diffusion then is allowed to vary between 0.01 m^2/s to 100 m^2/s which roughly correspond to the extreme cases of diffusion levels set by the classical and Bohm diffusion models respectively. The prior for the peaking ratio is then bound between -100 and 100 which allows for the model to explore both peaked and hollow impurity profiles over a wide range. Additionally, the transport in the edge is set to the ad-hoc values of D = 0.5 m^2/s and V = 0 m/s. This choice simplifies the simulation dynamics in the SOL since, following introduction via the source term, the number of impurities which reach the confined region will be gov-
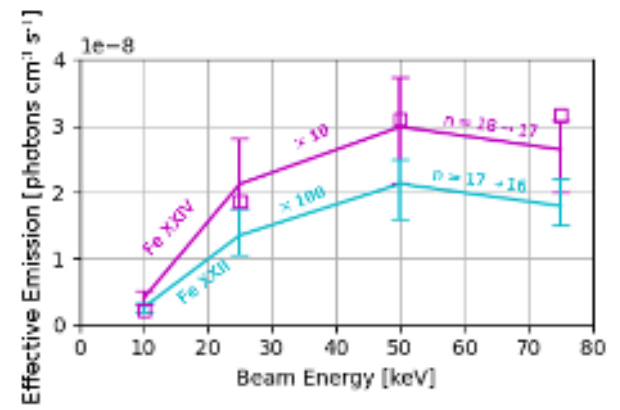

FIG. 4. Effective emission coefficients calculated for Fe^{22+} and Fe^{24+} for the transitions observed in figure 1. The data shown in hollow squares has been calculated previously using the ADAS code suite for Fe^{24+}.
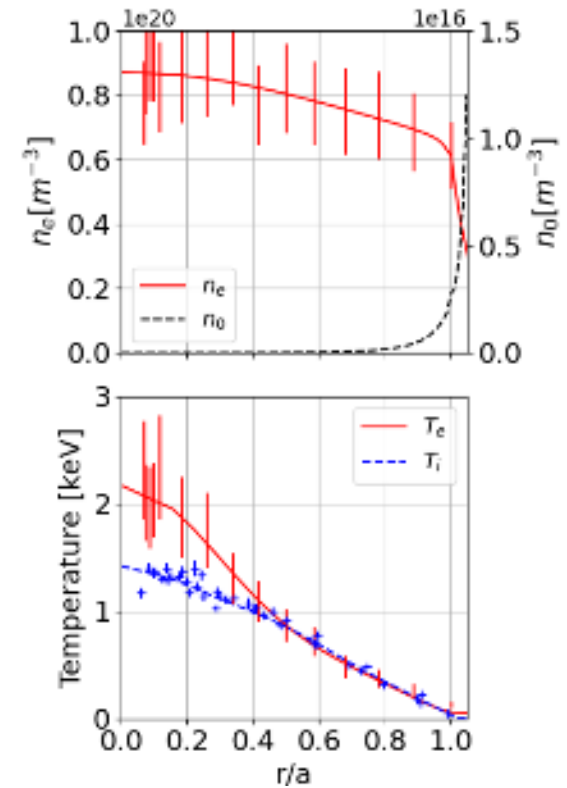

FIG. 5. Measured kinetic profiles for the analyzed W7-X discharge during the duration of the LBO injection.

erned by how fast they influx toward the LCFS due to diffusion and the rate at which they are lost to the divertor. To allow for enough flexibility to match the simulation to the diagnostic signals, this loss rate is included as an additional free parameter in the inference scheme and can vary between 100 s^{-1} and 10^8 s^{-1}. We also apply Jefferys prior to sample the impurity diffusion as well as the edge loss rate. This enforces uniform sampling in log
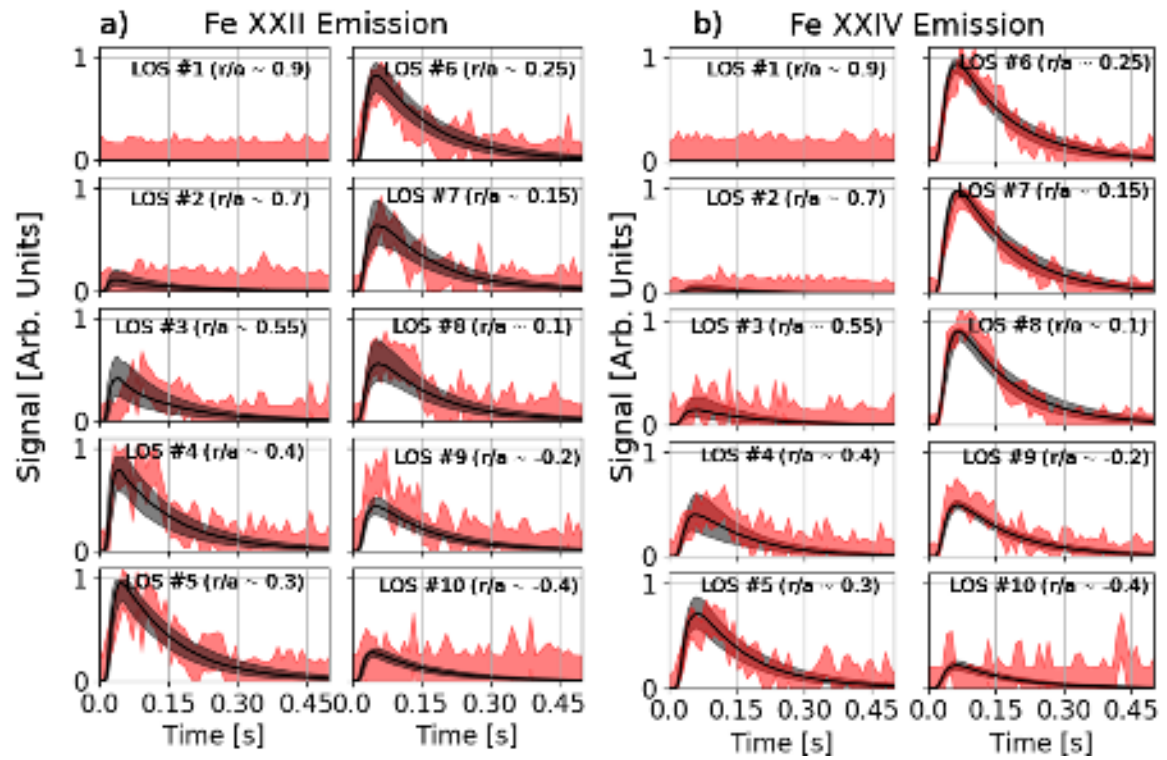
FIG. 6. Fitted CXRS emission from Fe XXII (a) and Fe XXIV (b) for all ten available lines of sight. Measurement uncertainty based on photon statistics is given in shaded red while the fitting uncertainty is given in shaded gray. Shown here is the results from the inference case where only the relatively calibrated CXRS signals are fitted

space allowing for the unbiased exploration over several orders of magnitude. Next, the likelihoods are assumed to be Gaussian with widths given by their experimental uncertainties and are combined using the independent likelihood pooling method[23].

Model uncertainties are also considered in the Bayesian framework. In practice, this can be accomplished by allowing the relevant inputs to the forward model to vary according to their levels of uncertainty and including them as so-called "nuisance" parameters in the inference. The background electron temperature has the strongest effect on the impurity ionization/recombination rates and therefore the T_e profile is allowed to vary within the error bars depicted in figure 5. For each sampled temperature profile, the impurity ionization and recombination rates are determined from ADAS tabulated values. Additionally, the beam attenuation, and therefore the density of neutrals along the sight-lines depends strongly on the electron density profile. To include the effect of the uncertainty in n_e, the beam attenuation is evaluated using pyFIDASIM for the case of an n_e profile scaled either up or down based on the error bars shown in figure 5. This gives two extremes for the possible beam attenuation. The Bayesian inference scheme then chooses a sample beam attenuation profile which is between these two bounds. Once a set of kinetic profiles is sampled and the ADAS rate coefficients for ionization, recombination, and radiated power are determined, an additional
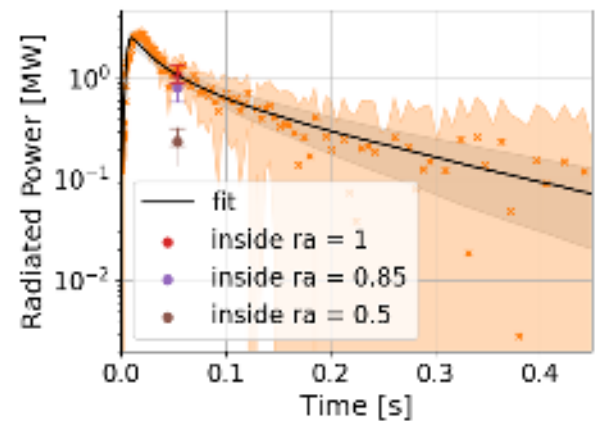

FIG. 7. Radiated power measured inside the LCFS shown with orange Xs with measurement uncertainty shown in shaded orange. Radiation fraction measurements are shown with the error bars. Fitted total radiated power is shown in black with shaded grey depicting the fitting uncertainty. Fitted radiation fractions are shown in the colored circles. Shown here is the results from the inference case where both the bolometer and the CXRS signals are fitted.

uncertainty of 15% in the rates themselves is considered based on previously reported estimates of their expected error[24]. The uncertainty in the rate coefficients is assumed to be independent for each process (i.e. ACD,
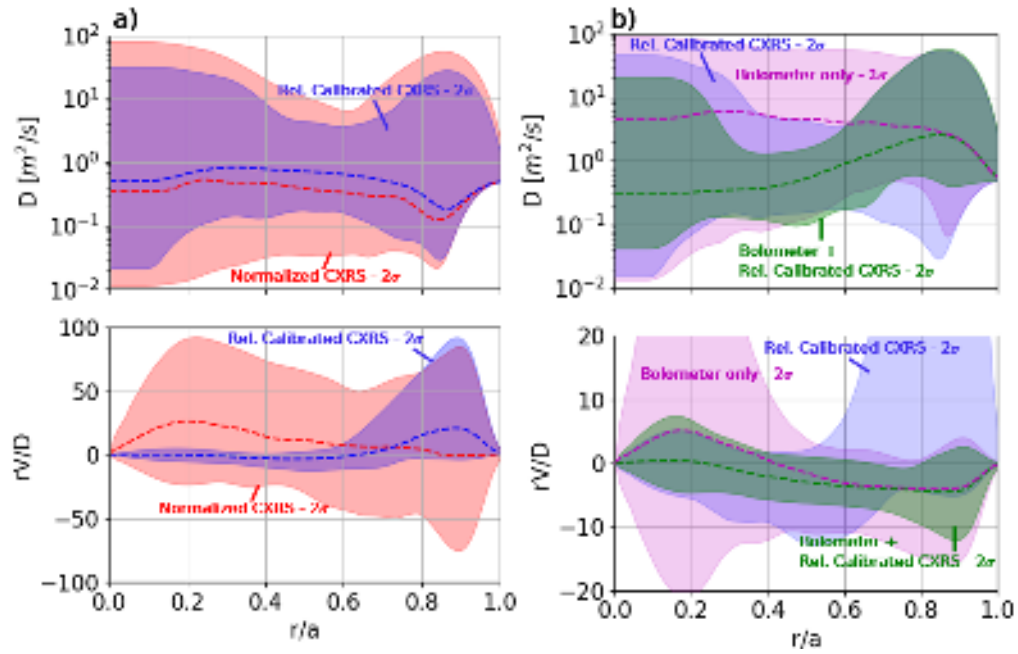
FIG. 8. Inferred impurity diffusion and convection profiles with the median profile sample are shown by the dashed line and the two-sigma error bars are shown in shaded color. a) depicts the comparison between the inference considering each CXRS signal normalized to 1 and the case where the relative intensity between lines of sight is considered. b) shows the inferred transport profiles for the case of considering the bolometer measurements by themselves and when included along with the relatively calibrated CXRS signals. Additionally shown is inference result considering relatively calibrated CXRS signals to depict the improvement in uncertainty.

SCD, CCD, PLT, PRB, and PRC coefficients which correspond to, in order, the effective recombination, ionization, and charge exchange coefficients as well as the radiated power cooling rate coefficients for line emissions, recombination+Bremsstrahlung, and charge exchange). Finally, the inference parameters are sampled using the markov chain monte carlo method to determine the structure of the posterior distribution[25].

V. INFERENCE RESULTS

A representative NBI heated W7-X plasma in which LBO injections have been carried out is chosen for analysis (discharge #20230314.26). The plasma conditions are generated via 2.3 MW of electron cyclotron resonance heating (ECRH) and 2 MW of NBI heating in the "high-mirror" configuration[26]. Kinetic profiles measured at the time of the impurity injection are given in figure 5 and are determined via a combination of Thomson scattering[27] and CXRS measurements of intrinsic carbon[28]. Also shown in figure 5 is a neutral density profile that has been calculated via the pyFIDASIM code similar to the method described in 9. 22.5 seconds into the discharge, an LBO injection of $\sim 10^{17}$ particles is performed following which impurity radiation is observed.

Measured and fitted CXRS signals are shown in figure 6 with the corresponding fitted transport profiles shown

in figure 8. The fit is performed for the case where the line emissions seen by each line of sight is normalized to a maximum intensity of 1 as well as the case where the intensity calibration is applied to compare the relative intensity of each line of sight (as is shown in figure 6). The fitted transport profiles along with the 2 sigma error bands are given in figure 8a. The fitted signals agree very well with measurements with the exception of the time characteristic of the Fe XXII signal seen along sight-line 3. This could be explained by a brief reduction in the overall electron temperature immediately following the impurity injection, which is seen to recover after ~ 15 ms. This affects the outer lines of sight most severely since the Fe^{21+} ionization rate decreases dramatically below ~ 500 eV.

Here we can see that by including the information from the relative intensity of the CXRS signals, the error bars on the inferred transport parameters are reduced significantly, particularily in the impurity peaking ratio. Additionally, it is apparent that the uncertainty increases significantly in the edge region, outside of where reliable Fe XXII and Fe XXIV emission is seen.

Despite the significant improvement by considering the relative intensities of the CXRS signals, this data alone cannot constrain the impurity peaking ratio well enough to distinguish between positive and negative peaking, especially in the edge. However, by combining the CXRS data with additional impurity measurements, it is pos-

sible to constrain the inferred peaking ratio more than would be possible with either of the two diagnostics when considering them independently. Here, we choose to combine the CXRS data with total radiated power measurements captured by a metal foil bolometry system[29] since the total radiated power provides a constraint on the total modeled impurity content which is strongly affected by the transport near the edge.

The volume-integrated radiated power can be determined from tomographic inversion of the individual bolometer lines of sight and can provide constraints on the total number of injected impurities which reach the confined region. These tomographic inversions of both the total radiated power inside of the LCFS as well as radiation fractions inside of r/a = 0.85 and 0.5 are available. The former is collected at a frame rate of 600 Hz with the latter collected at 15 Hz. To simulate the radiation from the impurity species, ADAS cooling rate coefficients[30] are utilized alongside the pySTRAHL calculated impurity densities:

$$P(t) = \int \int \int \sum_Z n_Z(\frac{r}{a}, t) \left(n_e(\frac{r}{a}) \left(PLT + PRB \right) \right.$$
$$\left. + \langle n_0 \rangle (\frac{r}{a}) PRC \right) dV \tag{7}$$

Again, PLT, PRB, and PRC indicate the effective radiated power coefficients for impact excitation, recombination, and charge exchange contributions respectively. $\langle n_0 \rangle$ represents the flux surface averaged neutral density. n_Z represents the impurity density for charge state Z which is calculated via the pySTRAHL code. Note that since the modeled signals only consider radiation from the injected iron, the background plasma radiation levels are subtracted from the experimental signals to isolate the response from the injection.

Figure 7 shows the fitted radiated power measurements along with the fitted radiation fractions when included in the inference with the CXRS signals. The fitted transport profiles and two-sigma error bands for the case of fitting only the bolometer measurements as well as the bolometer+CXRS measurements are given in figure 8b. Note the change in the y-axis bounds for the peaking ratio compared to figure 8a. Here one can see that the inclusion of the bolometer measurements in the framework provides a much stronger constraint on the peaking ratio compared to the CXRS signals alone. This is because, while the relatively calibrated CXRS measurements provide strong constraints on the density profile for Fe^{22+} and Fe^{24+}, they do not strongly constrain the total impurity density profile in the way that the bolometer radiation fraction measurements do.

VI.   CONCLUSION

In this work, we have shown the value of utilizing High-n Rydberg transitions for diagnosing impurity species in fusion plasmas since they are free of passive emission,

present over a wide wavelength range, and insensitive to the specific impurity element. Several of these transitions have already been observed in experiments and the strategies for identifying them throughout the visible spectrum have been discussed. Hundreds of these visible wavelength transitions are predicted to exist for a wide range of charge states and future experiments could investigate these for a variety of impurity emission-based experiments.

To model the emissions of these Rydberg transitions, a technique has been described for solving the steady state energy level population balance of the impurity ions which undergo charge exchange. This allows for the calculation of the effective emission coefficients necessary to quantify the signal intensity from the different beam energy components. This technique was then applied to calculate effective emission coefficients for experimentally observed transitions for which, data was previously unavailable. While the energy dependence of the calculated emission coefficients reproduces those found on the OPEN-ADAS database, they can then only be trusted as well as the previous datasets. Experimental validation of the energy dependence could be performed by taking measurements with differing beam energies.

The Bayesian approach has been applied here to consider the effect of kinetic profile and atomic rate uncertainties while still allowing for statistically significant determination of impurity transport profiles. Additionally, the self consistent inclusion of radiated power measurements is shown to provide strong constraints on the impurity peaking ratio, and when paired with the CXRS signals give an inference of the impurity transport with error bars smaller than those determined when considering either of the diagnostics independently.

VII. BIBLIOGRAPHY

[1] W. Biel, A. Greiche, R. Burhenn, E. Jourdain, and D. Lepere, Review of Scientific Instruments **77** (2006), 10.1063/1.2221659.

[2] A. Langenberg *et al.*, Review of Scientific Instruments **89**, 10G101 (2018).

[3] P. Beiersdorfer, J. K. Lepson, M. Bitter, K. W. Hill, and L. Roquemore, Review of Scientific Instruments **79**, 10E318 (2008).

[4] M. L. Reinke, P. Beiersdorfer, N. T. Howard, E. W. Magee, Y. Podpaly, J. E. Rice, and J. L. Terry, Review of Scientific Instruments **81**, 10D736 (2010).

[5] A. Langenberg *et al.*, Nucl. Fusion **57** (2017), 10.1088/1741-4326/aa70f4.

[6] B. Geiger *et al.*, Nucl. Fusion **59** (2019), 10.1088/1741-4326/aaff71.

[7] F. Sciortino *et al.*, Plasma Physics and Controlled Fusion **64**, 124002 (2022).

[8] T. Romba, F. Reimold, R. Jaspers, O. Ford, L. Vanó, and T. Klinger, Nuclear Fusion **63**, 076023 (2023).

[9] C. Swee, B. Geiger, R. Dux, S. T. A. Kumar, J. F. Castillo, A. Bader, and M. Gerard, Plasma Physics and Controlled Fusion **64**, 015008 (2022).

[10] J. K. Lee, H. H. Lee, W. H. Ko, B. Na, J. Ko, M. W. Lee, and S. G. Lee, AIP Advances **12**, 055111 (2022).

[11] B. C. Stratton *et al.*, Nucl. Fusion **31**, 171 (1991).

[12] C. Swee, B. Geiger, R. Albosta, O. Ford, S. Loch, M. D. Nornberg, J. Schellpheffer, and T. Wegner, Review of Scientific Instruments **93** (2022), 10.1063/5.0101842.

[13] C. Swee *et al.*, Nucl. Fusion (2024 under review).

[14] T. Wegner *et al.*, Review of Scientific Instruments **89** (2018), 10.1063/1.5037543.

[15] T. Wegner and F. Kunkel, Fusion Engineering and Design **193**, 113691 (2023).

[16] E. Haug, Modern Physics **11** (2020).

[17] R. E. Olson, Physical Review A **24**, 1726 (1981).

[18] A. Thorman *et al.*, Physica Scripta **96**, 125631 (2021).

[19] B. Geiger *et al.*, Plasma Physics and Controlled Fusion (2020).

[20] R. McDermott, R. Dux, F. Guzman, T. Pütterich, R. Fischer, A. Kappatou, and the ASDEX Upgrade team, Nuclear Fusion **61**, 016019 (2020).

[21] A. Foster, *On the behaviour and radiating properties of heavy elements in Fusion Plasmas*, Ph.D. thesis, University of Strathclyde (2009).

[22] N. R. Badnell, Journal of Physics B: Atomic and Molecular Physics **19**, 3827 (1986).

[23] U. Von Toussaint, Rev. Mod. Phys. **83**, 943 (2011).

[24] S. N. Nahar, A. K. Pradhan, and H. L. Zhang, The Astrophysical Journal Supplement Series **133**, 255 (2001).

[25] D. Foreman-Mackey, D. W. Hogg, D. Lang, and J. Goodman, Publ. Astron. Soc. Pac. **125**, 306 (2013).

[26] A. Dinklage and et al., Nature Physics **14**, 855–860 (2018).

[27] E. Pasch, M. N. A. Beurskens, S. A. Bozhenkov, G. Fuchert, J. Knauer, R. C. Wolf, and W.-X. Team, Review of Scientific Instruments **87**, 11E729 (2016).

[28] O. P. Ford *et al.*, Review of Scientific Instruments **91** (2020), 10.1063/1.5132936.

[29] D. Zhang *et al.*, Nuclear Fusion **61**, 116043 (2021).

[30] H. P. Summers, W. J. Dickson, M. G. O'Mullane, N. R. Badnell, A. D. Whiteford, D. H. Brooks, J. Lang, S. D. Loch, and D. C. Griffin, Plasma Physics and Controlled Fusion **48**, 263 (2006).